ACS APPLIED MATERIALS & INTERFACES

Research Article

www.acsami.org

Understanding Structure–Function Relationship in Hybrid Co_3O_4–Fe_2O_3/C Lithium-Ion Battery Electrodes

Irin Sultana,[†] Md Mokhlesur Rahman,[*,†] Thrinathreddy Ramireddy,[†] Neeraj Sharma,[‡] Debasis Poddar,[†] Abbas Khalid,[§] Hongzhou Zhang,[§] Ying Chen,[†] and Alexey M. Glushenkov[*,†,∥]

[†]Institute for Frontier Materials, Deakin University, Waurn Ponds, Victoria 3216, Australia

[‡]School of Chemistry, University of New South Wales, Sydney, New South Wales 2052, Australia

[§]School of Physics and Centre for Research on Adaptive Nanostructures and Nanodevices (CRANN), Trinity College Dublin, Dublin 2, Ireland

[∥]Melbourne Centre for Nanofabrication, 151 Wellington Rd., Clayton, Victoria 3168, Australia

Supporting Information

ABSTRACT: A range of high-capacity Li-ion anode materials (conversion reactions with lithium) suffer from poor cycling stability and limited high-rate performance. These issues can be addressed through hybridization of multiple nanostructured components in an electrode. Using a Co_3O_4–Fe_2O_3/C system as an example, we demonstrate that the cycling stability and rate performance are improved in a hybrid electrode. The hybrid Co_3O_4–Fe_2O_3/C electrode exhibits long-term cycling stability (300 cycles) at a moderate current rate with a retained capacity of approximately 700 mAh g^{-1}. The reversible capacity of the Co_3O_4–Fe_2O_3/C electrode is still about 400 mAh g^{-1} (above the theoretical capacity of graphite) at a high current rate of ca. 3 A g^{-1}, whereas Co_3O_4–Fe_2O_3, Fe_2O_3/C, and Co_3O_4/C electrodes (used as controls) are unable to operate as effectively under identical testing conditions. To understand the structure–function relationship in the hybrid electrode and the reasons for the enhanced cycling stability, we employed a combination of ex situ and in situ techniques. Our results indicate that the improvements in the hybrid electrode originate from the combination of sequential electrochemical activity of the transition metal oxides with an enhanced electronic conductivity provided by percolating carbon chains.

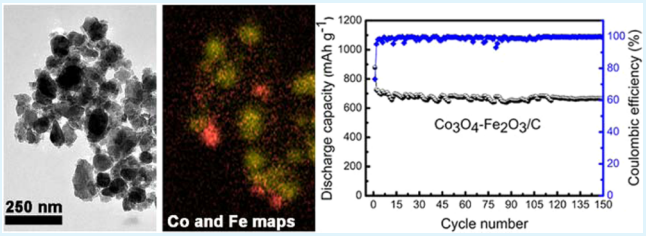

KEYWORDS: *hybrid electrodes, cycling stability, in situ synchrotron XRD, ex situ SEM, Li-ion batteries*

1. INTRODUCTION

Hybridization is emerging as an innovative concept in the field of electrochemical energy storage. The idea is to include dissimilar (in terms of composition, performance or function) components into an energy storage device.[1] This may be implemented in the form of creating hybrid devices (e.g., Li-ion capacitors, supercapbatteries, and hybrid asymmetric capacitors) via combining two electrodes of different types (e.g., a battery-type electrode with a capacitive electrode).[2,3] Another variation of the hybridization concept, as emphasized by recent reviews,[1,4] is to include dissimilar nanostructured components within a single electrode of a battery or capacitor. By incorporating a combination of materials in a single electrode, electrochemical performance can be improved in many cases. One possible type of battery electrode in which the hybridization concept could be effectively used is lithium-ion battery anodes that operate via conversion reaction mechanisms.

Conversion reaction anodes (transition metal oxides are the most common examples)[5,6] have been attracting considerable attention over the past decade. Transition metal oxides (TMOs), in particular 3d TMOs, are found to be potential replacements of graphite as anode materials in Li-ion batteries due to their very high specific capacity. The mechanism of reaction with lithium is different from that of the carbon-based materials. Lithium ions react reversibly with metal oxides via a conversion reaction that involves the formation and decomposition of Li_2O and is accompanied by the reduction and oxidation of metal nanoparticles. Generally, the electrochemical reactions can be summarized by the following equation:[7,8]

$$M_xO_y + 2yLi^+ + 2ye^- \leftrightarrow yLi_2O + xM \quad (1)$$

The forward reaction is thermodynamically favorable and involves multiple electron transfer per unit of metal atom leading to a high theoretical lithium storage capacity (400–1100 mAh g^{-1}).[5] However, the realization of a practical battery with TMO anodes that undergo reversible conversion reactions during cycling is not straightforward. The oxides reacting electrochemically with lithium through conversion reactions often experience significant volume changes upon lithiation and

Received: June 25, 2015
Accepted: September 4, 2015
Published: September 4, 2015

DOI: 10.1021/acsami.5b05658
ACS Appl. Mater. Interfaces 2015, 7, 20736–20744

delithiation (for example, volume changes for cobalt oxide (Co_3O_4, theoretical capacity of 980 mAh g^{-1} [9,10]) and hematite iron oxide (α-Fe_2O_3, theoretical capacity of 1007 mAh g^{-1} [11−13]) are as high as ∼100 and ∼96%, respectively[14−16]). Such a significant volume variation routinely results in pulverization and cracking of electrodes in the battery due to the internal stress in the electrode and the lack of space for expansion. As a result, stable cyclic behavior and good rate capability are difficult to achieve in conversion reaction anodes. In addition, many of the oxide phases that react through conversion reactions possess limited electronic conductivity. To circumvent these problems, the hybridization concept is widely used, and electrochemical performance, especially reversible capacity of the respective TMO anodes, is improved significantly.[17−20]

Despite the success of hybridization of TMOs, progress in understanding the fundamental electrochemistry of the hybrid electrodes has been slow. A battery is a complex device where many concurrent events occur during its operation, which makes it difficult to understand the intrinsic electrochemistry. Therefore, a fundamental understanding of the structural stability of the hybrid electrode during cycling is important and can provide insights about electrochemical reactivity of the electrode and the performance of the battery as a whole. Currently, many aspects of the fundamental science with respect to battery operation remain poorly understood, and the electrochemical lithiation/delithiation mechanism can be considered as one of these for many electrode materials.[21]

Herein, we report an improved cycling stability and rate performance of a hybrid Co_3O_4−Fe_2O_3/C electrode with respect to control systems (Co_3O_4−Fe_2O_3, Co_3O_4/C, and Fe_2O_3/C electrodes). The electrochemical performance of this hybrid material is analyzed, and a combination of ex situ and in situ techniques is employed to understand the correlation between the structure and performance of the material. An in situ structural study is achieved using synchrotron X-ray diffraction (XRD) under electrochemical conditions. These in situ synchrotron XRD data illustrate the structural changes during battery operation in real time. The experimental results suggest that both components of Co_3O_4 and Fe_2O_3 in the hybrid are electrochemically active but at different potentials. The combination of two transition metal oxides in the electrode leads to their sequential volume expansion (and, therefore, better tolerance of the electrode to structural stress) while long conductive chains of carbon black act as a percolating network suitable for the efficient electronic transfer (and, presumably, spacing of the nanoparticles for expansion/contraction during operation).

2. EXPERIMENTAL SECTION

2.1. Synthesis of Materials. Co_3O_4−Fe_2O_3/C, Co_3O_4−Fe_2O_3, Co_3O_4/C, and Fe_2O_3/C materials were synthesized by the molten salts method (a brief introduction is included in Supporting Information). The Co_3O_4−Fe_2O_3 powder was produced by mixing together $CoCl_2 \cdot 6H_2O$ (Sigma-Aldrich, 98%), $FeCl_2 \cdot 4H_2O$ (Sigma-Aldrich, 98%), $LiNO_3$ (Sigma-Aldrich, 99.9%), $LiOH \cdot H_2O$ (Sigma-Aldrich, 98%), and H_2O_2 (Sigma-Aldrich, 35%) with a molar ratio of 1:1:10:2:5, respectively, followed by grinding the mixture in a mortar with a pestle until homogeneous. This was designed to provide a 50:50 mix of Co_3O_4/Fe_2O_3 for the Co_3O_4−Fe_2O_3 material. The mixture was immediately transferred to a muffle furnace and heat treated in air at 300 °C for 3 h. After cooling naturally in air, the solid mass was washed with a large amount of DI water to dissolve unreacted salts and Co_3O_4−Fe_2O_3 solid particles were separated by centrifugation. The product was then dried under vacuum at 100 °C overnight to remove the residual water.

Hybrid Co_3O_4−Fe_2O_3/C materials were prepared by mixing Co_3O_4−Fe_2O_3 materials synthesized by the molten salt method and super P Li carbon black powder in a 2:1 weight ratio. Then, 4.5 g of the mixture was loaded inside a stainless steel milling container together with four hardened steel balls (diameter of 25.4 mm). The mixture was milled in a magneto-ball mill at a rotation speed of 75 rpm for 30 h at room temperature under an argon atmosphere of 100 kPa.[22,23] This type of mill is usually used in conjunction with an external magnet; however, the magnet was intentionally removed in the preparation procedure to ensure a rolling action of the balls. In addition, the rotation speed (75 rpm) was intentionally selected low to ensure gentle milling. The milled powders were removed from the ball milling containers in the presence of an inert Ar atmosphere. Co_3O_4/C and Fe_2O_3/C nanocomposites were prepared using procedures similar to described above. Co_3O_4 or Fe_2O_3 nanoparticles synthesized by the molten salt method and super P Li carbon black powder were mixed in a 2:1 weight ratio and 4.5 g of the mixture for each composite were used for this purpose.

2.2. Materials Characterization. X-ray diffraction (XRD, PANalytical X'Pert Pro) data were collected using a Cu$K\alpha$ radiation source (λ = 1.54181 Å). The morphology of each sample was examined using scanning electron microscopy (SEM, Carl Zeiss Supra 55 VP). Transmission electron microscopy (TEM) analysis was performed on a JEOL JEM 2100F instrument operated at 200 kV and an FEI Titan instrument operating at 300 kV. Elastic image and energy-filtered elemental maps were acquired using a Gatan Quantum ER 965 Imaging Filter installed on the JEOL JEM 2100F microscope, and a three-window method was used for acquiring elemental maps. Energy dispersive X-ray spectra (EDS) were acquired on the FEI Titan transmission microscope in a scanning transmisison mode.

2.3. Electrode Preparation. To test the electrochemical performance, we mixed powder samples with acetylene carbon black (AB) and a binder, carboxymethyl cellulose (CMC), in a weight ratio of 80:10:10 in a solvent (distilled water). The as-prepared slurry was spread onto Cu foil substrates with an average loading of 1.5−2.0 mg and these coated electrodes were dried in a vacuum oven at 100 °C for 24 h. The electrode was then pressed using a 25 mm diameter disc to enhance the contact between the Cu foil and active material.

2.4. Ex Situ Electrochemical Characterization. The electrodes were cut to 1 × 1 cm and CR 2032 coin-type cells were assembled in an Ar-filled glovebox. Li foil was used as the counter/reference electrode and a microporous polyethylene film was used as a separator. The electrolyte was 1 M $LiPF_6$ in a mixture of ethylene carbonate (EC), diethylene carbonate (DEC), and dimethyl carbonate (DMC) with a volume ratio of 1:1:1. The cells were galvanostatically charged/discharged in the range of 3.0−0.01 V at different current densities using the Land Battery Testing System.

2.5. In Situ Electrochemical−Structural Characterization. For in situ electrochemical−structural characterization, special coin cell casings with 3 mm diameter holes and stainless spacers with 5 mm diameter holes were used for the construction of the coin cells. The cell casings were electrically insulated from the other components using Kapton tape, which also sealed the cell against air and allowed penetration of the X-ray beam. The coin cells contained active materials on the Cu foil (Co_3O_4−Fe_2O_3 sample was used) as the working electrode, Li metal as the counter/reference electrode, microporous polyethylene film as a separator and 1 M $LiPF_6$ (in a mixture of EC, DEC, and DMC with a volume ratio of 1:1:1) as an electrolyte solution. In situ synchrotron XRD experiments were performed within 1−2 days after cell construction. Further details regarding coin cell construction and beamline setup can be found in references.[24−28] In situ synchrotron XRD data were collected on the Powder Diffraction beamline at the Australian Synchrotron with a wavelength (λ) of 0.68829(2) Å,[29] determined using the NIST 660b LaB_6 standard reference material. Data were collected continuously in 6.4 min acquisitions on the coin cell in transmission geometry throughout the charge/discharge cycles. The coin cell was first discharged to 0.01 V at −0.45 mA (∼300 mA g^{-1}) followed by charge

DOI: 10.1021/acsami.5b05658
ACS Appl. Mater. Interfaces 2015, 7, 20736−20744

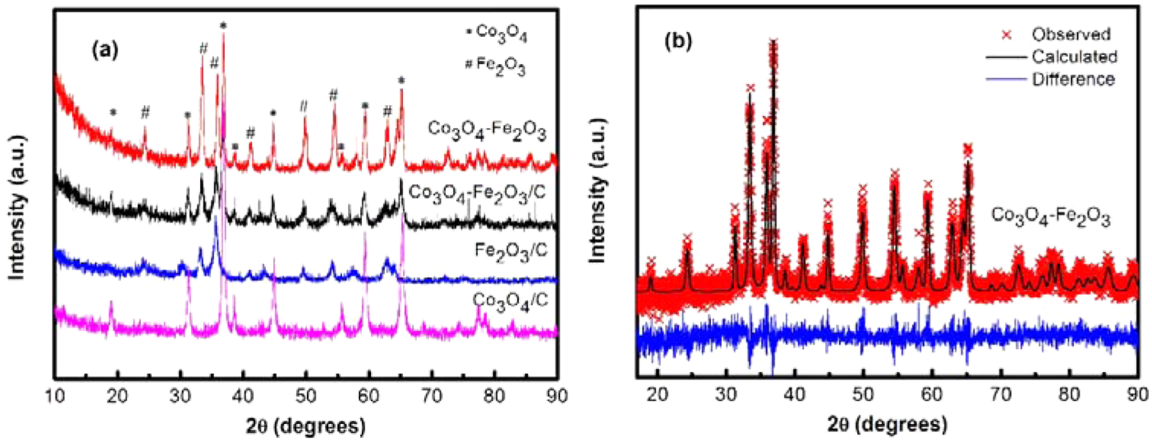

Figure 1. XRD patterns of (a) Co_3O_4–Fe_2O_3/C, Co_3O_4–Fe_2O_3, Co_3O_4/C, and Fe_2O_3/C materials; and (b) Rietveld-refined fit of the Co_3O_4 and Fe_2O_3 structural models to the XRD data for the Co_3O_4–Fe_2O_3 sample.

back to 3.0 V. Rietveld refinements were carried out using the GSAS[30] software suite with the EXPGUI[31] software interface.

3. RESULTS AND DISCUSSION

We produced four samples: a hybrid Co_3O_4–Fe_2O_3/C material and three control samples (Co_3O_4–Fe_2O_3, Co_3O_4/C, and Fe_2O_3/C) . The sample Co_3O_4–Fe_2O_3 represents a mixture of Co_3O_4 and Fe_2O_3 nanoparticles prior to their introduction in the carbon host. Samples of Fe_2O_3/C and Co_3O_4/C are nanoparticles and their aggregates of iron and cobalt oxides, respectively, introduced in the carbon host. More detailed characterization of control materials may be found in the Supporting Information. For initial characterization, XRD was carried out to study the crystalline structure and phase purity of the obtained products (Figure 1a). The hybrid sample shows a mixed-phase XRD pattern where diffraction peaks consistent with the cubic phase of Co_3O_4 [JCPDS no. 00-043-1003, space group $Fd\bar{3}m$ (no. 227)] and a rhombohedral phase of hematite α-Fe_2O_3 [JCPDS no. 01-072-6226, space group R-3c (no.167)] are observed. No peaks of any other phases or impurities were detected, demonstrating that materials with high purity could be obtained using the present synthesis strategy. The Co_3O_4–Fe_2O_3, Co_3O_4/C, and Fe_2O_3/C samples display XRD reflections of the corresponding oxides. Rietveld-refined fit of the Co_3O_4 and Fe_2O_3 structural models to the XRD data for the Co_3O_4–Fe_2O_3 sample is shown in Figure 1b. The refined relative phase fractions of Co_3O_4 and Fe_2O_3 were approximately 42 and 58 wt %, respectively, suggesting a slight excess of Fe_2O_3 in the crystalline components of the Co_3O_4–Fe_2O_3 sample.

TEM analysis was employed to visualize the structure of the hybrid material. Figure 2a shows a bright-field image of the hybrid Co_3O_4–Fe_2O_3/C sample and demonstrates the structure which consists of nanoparticles of Co_3O_4 and Fe_2O_3 (and, possibly, their aggregates) integrated into a network of chain-like carbon black. The oxide nanoparticles have a darker contrast in the image. An overlay of energy-filtered elemental maps of Co and Fe in the same location on the sample is shown in Figure 2b, demonstrating the distribution of the two oxides. The coexistence of Co_3O_4 and Fe_2O_3 nanoparticles supported on carbon was also cross-verified by EDS mapping at a different location. A bright field TEM image and a corresponding overlay of Co and Fe elemental maps are presented in Figure 2c,d. It is clearly seen that both Co_3O_4 and Fe_2O_3 particles are spread on

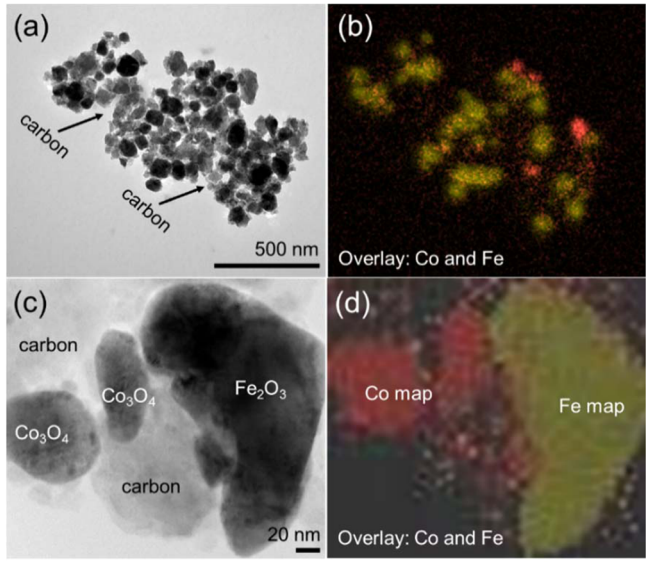

Figure 2. TEM characterization of the hybrid Co_3O_4–Fe_2O_3/C sample: (a and b) a bright–field image and the corresponding energy-filtered map of Co and Fe; (c and d) an image and a corresponding EDS map of Co and Fe from a different location; (red) Co, (green) Fe.

the carbon host and embedded into it. TEM characterization of the Co_3O_4–Fe_2O_3, Fe_2O_3/C, and Co_3O_4/C samples can be found in Supporting Information (Figure S1).

The electrochemical properties of the hybrid Co_3O_4–Fe_2O_3/C material are presented in Figure 3. The data on the cycling stabilities and rate capabilities of Co_3O_4–Fe_2O_3, Fe_2O_3/C, Co_3O_4/C samples are also shown. As shown in Figure 3a, a significant difference is observed in cycling stability among the electrodes. The hybrid Co_3O_4–Fe_2O_3/C electrode exhibits outstanding cycling stability at the 0.5C rate with a retained reversible capacity of 703 mAh g^{-1} (96% retention of the calculated theoretical capacity of 731 mAh g^{-1}) after 300 cycles. The cycling stability of the Co_3O_4–Fe_2O_3 electrode was observed to be significantly hampered at the 0.5C rate and the capacity fade was rapid resulting in a capacity of below 372 mAh g^{-1} after 42 cycles. Capacity fading was also observed for both Co_3O_4/C and Fe_2O_3/C electrodes at the 0.5C rate. In the case of Co_3O_4/C electrode, reversible capacity was 411 mAh g^{-1} (~60% retention of the calculated theoretical capacity of

DOI: 10.1021/acsami.5b05658
ACS Appl. Mater. Interfaces 2015, 7, 20736–20744

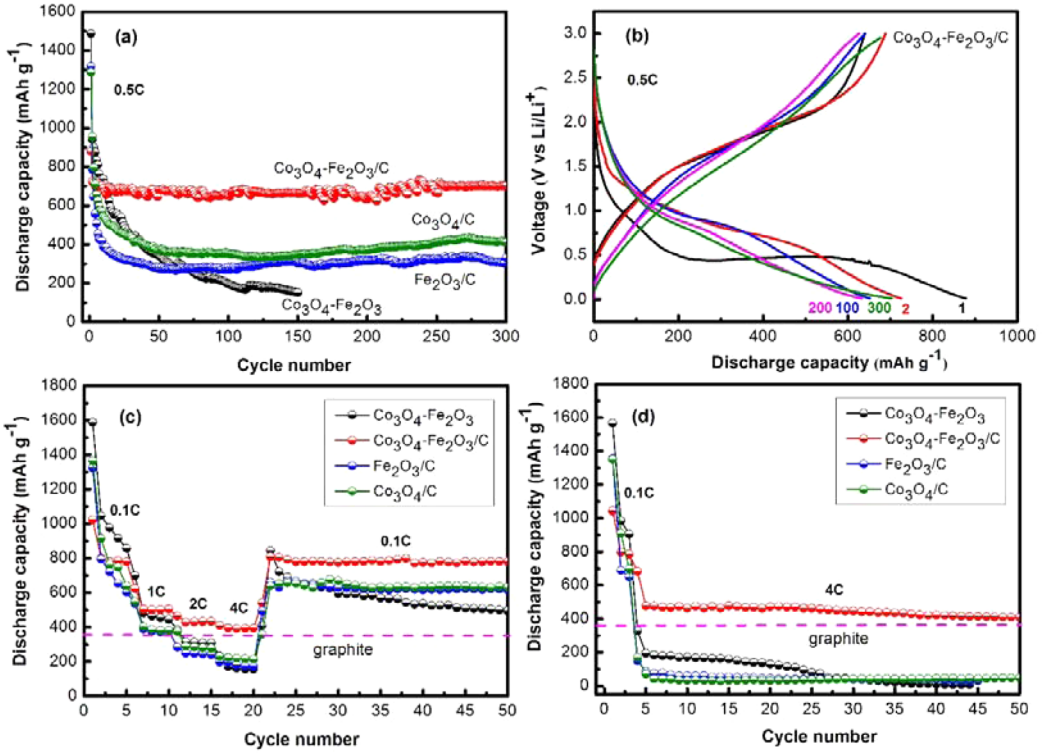

Figure 3. Electrochemical performance of the Co_3O_4–Fe_2O_3/C hybrid sample and the control samples (Co_3O_4–Fe_2O_3, Fe_2O_3/C and Co_3O_4/C): (a) cycling behavior at 0.5C rate; (b) charge/discharge profiles of the Co_3O_4–Fe_2O_3/C electrode in various cycles at 0.5C rate; (c) rate capability tests (current density changes from very low to moderate to very high and finally back to very low); and (d) rate capability tests (current density changes from very low to very high).

686 mAh g^{-1}) after 300 cycles, whereas it was only 330 mAh g^{-1} (43% retention of the calculated theoretical capacity of 764 mAh g^{-1}) for the Fe_2O_3/C electrode. The method for calculating theoretical capacity and C-rates is described in Supporting Information.

Figure 3b shows charge/discharge profiles of the hybrid Co_3O_4–Fe_2O_3/C electrode at 0.5C rate (the charge–discharge profiles for other samples can be found in Supporting Information, Figure S3). A relatively small irreversible capacity loss (about 26%) was observed in the first cycle. The capacity remains quite stable over 300 cycles, with minor changes in the shape of charge–discharge profiles. The Coulombic efficiency was close to 100% after the first few cycles (Supporting Information, Figure S4). Figure 3c demonstrates the consecutive cycling performance at different current rates, measured for five cycles at each current in ascending steps from 0.1C to 4C, followed by a return to 0.1C. The hybrid Co_3O_4–Fe_2O_3/C electrode exhibits the reversible capacities of 782, 505, 434, and 395 mAh g^{-1} at the current rates of 0.1, 1.0, 2.0, and 4C, respectively. As the rate is brought back to 0.1C, the reversible capacity of the Co_3O_4–Fe_2O_3/C electrode was still 780 mAh g^{-1} even after 50 cycles, which represents >99% capacity recovery with respect to the capacity of 782 mAh g^{-1} obtained after 5 cycles at 0.1C initially. It is clearly seen that Co_3O_4–Fe_2O_3, Fe_2O_3/C, and Co_3O_4/C electrodes experience significant capacity fading and capacity recovery after 50 cycles was unsatisfactory.

To further verify the high rate performance of hybrid Co_3O_4–Fe_2O_3/C electrode, we have demonstrated consecutive cycling performance at a low current rate (0.1C) followed by a very high rate (4C) (Figure 3d). For this purpose, all electrodes were cycled at the 0.1C rate for the initial three cycles, and in the subsequent cycles, the discharge/charge was set to the 4C rate. Surprisingly, the hybrid Co_3O_4–Fe_2O_3/C electrode is still capable to tolerate such a quick current rate transformation and even after 50 cycles reversible capacity was measured to be 410 mAh g^{-1} at 4C. As it follows from the electrochemical assessment, the cycling performance and rate capability of the hybrid Co_3O_4–Fe_2O_3/C are significantly superior to the electrodes made from other samples.

The hybrid Co_3O_4–Fe_2O_3/C electrode simultaneously demonstrates capacity retention, excellent rate capability and reasonably high reversible capacity. To date, only few attempts of hybridization of Co_3O_4 and Fe_2O_3 into hybrid Co_3O_4–Fe_2O_3 electrodes have been explored.[20,32,33] Wu et al.[20] have reported the direct growth of Co_3O_4/α-Fe_2O_3 branched nanowire heterostructures on a Ti substrate by a two-step hydrothermal method. Compared to pristine Co_3O_4 and α-Fe_2O_3 nanowires, lithium-ion battery anodes made of these Co_3O_4/α-Fe_2O_3 branched nanowires exhibit significantly enhanced Li^+ storage capacity and stability, with a high reversible capacity of 980 mAh g^{-1} after 60 cycles at a current density of 100 mA g^{-1}. Although the reversible capacity is attractive in this study, the capacity retention is unsatisfactory (~63%) with respect to the initial capacity (1534 mAh g^{-1}). Rate capability was not examined for this system. A hierarchical Fe_2O_3@Co_3O_4 nanowire array based on the sacrificial template accelerated hydrolysis (using ZnO as the template) has also been reported.[32] The Fe_2O_3@Co_3O_4 nanowire array exhibits good cycling performance (1005 mAh g^{-1} after 50 cycles at 200 mA g^{-1}) with improved rate performance (788 mAh g^{-1} at 5000 mA g^{-1}) but significant capacity fading can be observed. Recently, Luo et al.[33] demonstrated novel hierarchical Co_3O_4@α-Fe_2O_3 core–shell nanoneedle arrays (Co_3O_4@α-Fe_2O_3 NAs)

DOI: 10.1021/acsami.5b05658
ACS Appl. Mater. Interfaces 2015, 7, 20736–20744

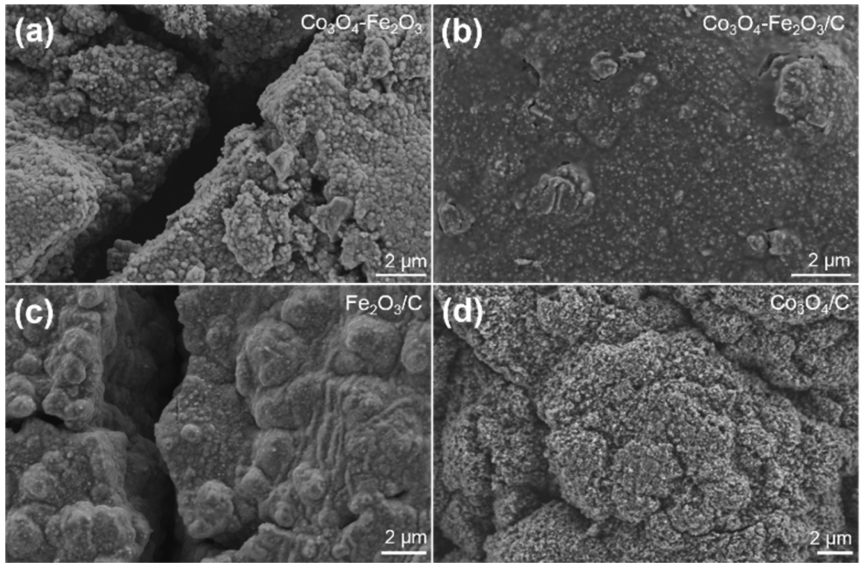

Figure 4. SEM images of the electrodes extracted from lithium half-cells after 50 cycles of rate capability test depicted in Figure 3c: Images of Co_3O_4–Fe_2O_3 (a), Co_3O_4–Fe_2O_3/C (b), Fe_2O_3/C (c) and Co_3O_4/C (d) electrodes are shown.

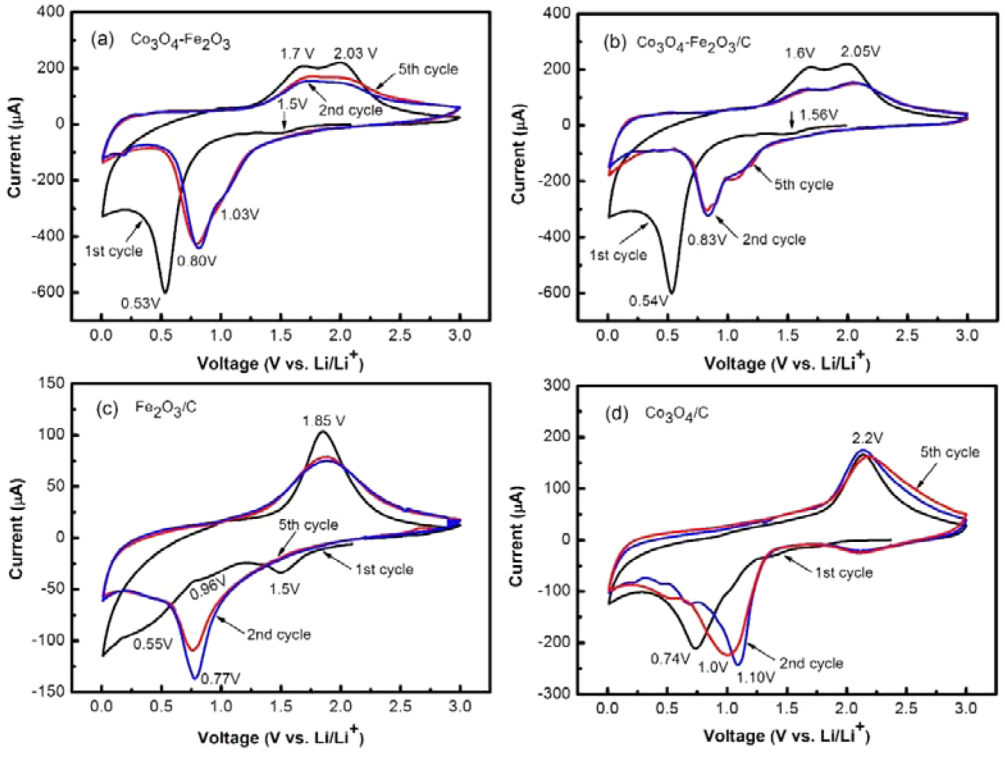

Figure 5. Cyclic voltammograms of (a) Co_3O_4–Fe_2O_3, (b) Co_3O_4–Fe_2O_3/C, (c) Fe_2O_3/C, and (d) Co_3O_4/C electrodes in the first, second, and fifth cycles in the voltage range of 0.01–3.0 V. Two pairs of reduction and oxidation peaks are visible in the CV plots of Co_3O_4–Fe_2O_3 and Co_3O_4–Fe_2O_3/C materials from the second cycle onward, indicating that maximum electrochemical activity in the Co_3O_4 and Fe_2O_3 components of the electrode happens at different potentials (causing sequential volume expansion-contraction in the components of the electrode).

produced by a stepwise, seed-assisted, hydrothermal approach. Compared to pristine Co_3O_4 NAs and α-Fe_2O_3 nanosheets, the Co_3O_4@α-Fe_2O_3 NAs show a high reversible capacity of 1045 mAh g^{-1} after the 100 cycles at 120 mA g^{-1}. This is the best reported result (in terms of reversible capacity) for the Co_3O_4–Fe_2O_3 anodes so far. However, the capacity retention (~53%) and rate capability are not satisfactory. It follows from the literature analysis that the electrochemical performance of the hybrid Co_3O_4–Fe_2O_3/C material reported here is attractive in respect to the previously published Co_3O_4–Fe_2O_3 based electrodes, especially due to the capacity retention and rate capability offered by the hybrid electrodes reported here.[20,32,33]

To gain insight into the improved performance of the hybrid Co_3O_4–Fe_2O_3/C electrode and the structure–function relationship of the material, we conducted a number of ex situ and in situ characterization tests. As it follows from the electrochemical assessment, the cycling performance and rate capability of the hybrid Co_3O_4–Fe_2O_3/C are significantly

DOI: 10.1021/acsami.5b05658
ACS Appl. Mater. Interfaces 2015, 7, 20736–20744

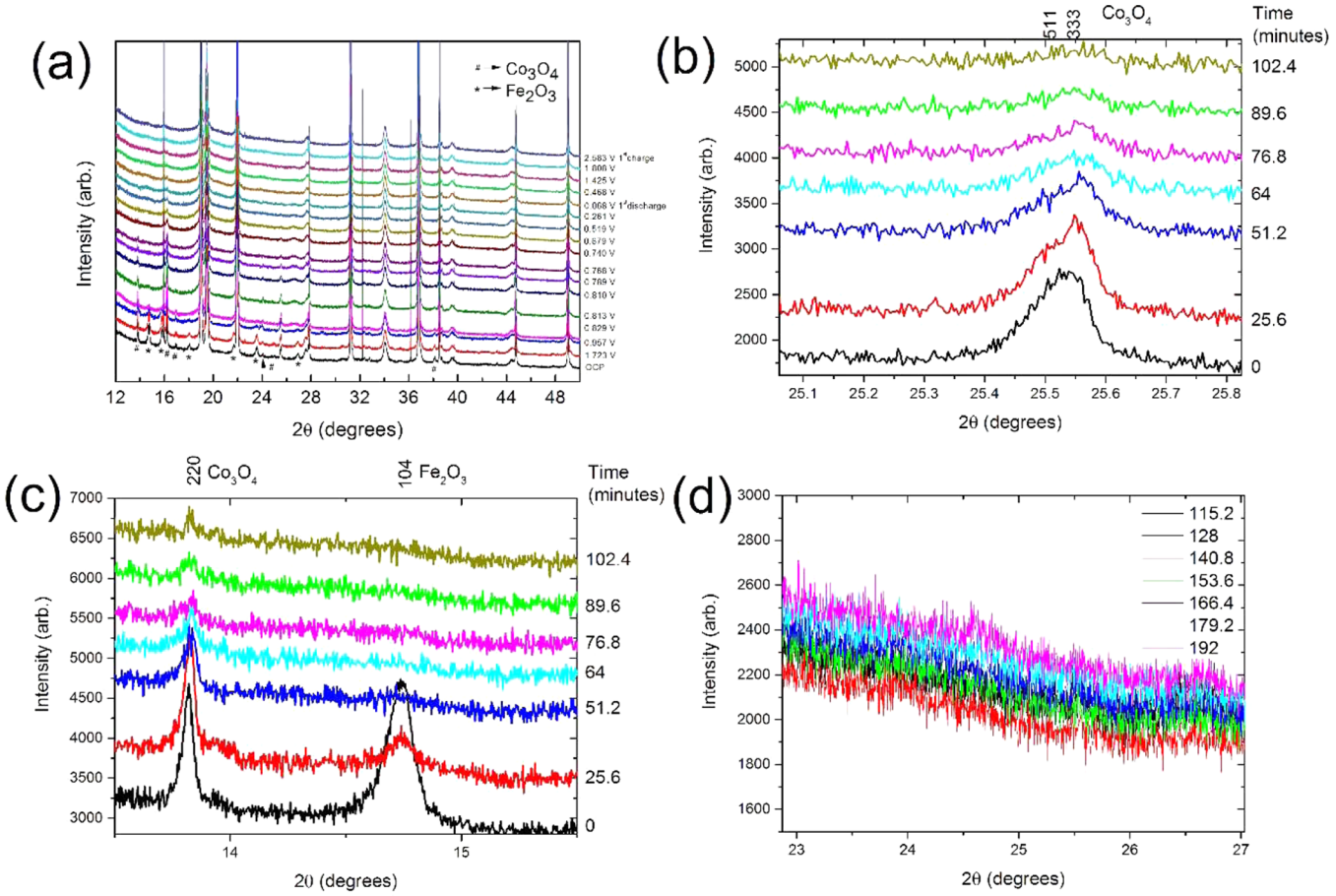

Figure 6. (a) In situ synchrotron XRD data of a Co_3O_4–Fe_2O_3 sample at various voltages; snapshots via stacked plots of the in situ data of the (b) 511, 333 Co_3O_4 and (c) 220 Co_3O_4 and 104 Fe_2O_3 reflections with time shown on the right-hand side of each graph; and (d) snapshots via a plot of the in situ data during the latter parts of the electrochemical cycle showing minimal change in the diffraction patterns. Note that in panel d, the data are shown as raw collections without stacking.

superior to the electrodes made from other samples. These improvements originate from the combination of the two oxides in the material and also the presence of the percolating carbon host. The role of the carbon host is quite obvious as it forms a conducting network resulting in more efficient electronic transport in the electrode. The combination of the two oxides is critical for the stress management in the electrode. Figure 4 shows the SEM images of the electrodes extracted after 50 cycles of galvanostatic discharge/charge with the sequence of the 50 cycles following the progressive rate increase (0.1, 1.0, 2.0, 4C) and the final current rate of 0.1C (i.e., the test is the same as the rate capability test depicted in Figure 3c). Clearly, the Co_3O_4–Fe_2O_3 and Fe_2O_3/C electrodes develop large cracks and their structural stability is compromised (Figure 4a,c). The Co_3O_4 electrode is more robust but minor cracks are still present after cycling, resulting in the deterioration in performance (Figure 4d). In contrast, no obvious cracks are visible in the hybrid Co_3O_4–Fe_2O_3/C electrode. This clearly demonstrates that the structural stability of the hybrid Co_3O_4–Fe_2O_3/C electrode is significantly better, resulting in its excellent cycling performance observed in this study.

The improved cycling stability of the hybrid Co_3O_4–Fe_2O_3/C electrode is related, in our view, to the sequential volume expansion in the Co_3O_4 and Fe_2O_3 components of the electrode. This can easily be understood from the analysis of the CV plots (Figure 5) and from the data of in situ XRD presented next. The CV plots of Co_3O_4–Fe_2O_3, Co_3O_4–Fe_2O_3/C, Fe_2O_3/C, and Co_3O_4/C (d) electrodes are shown. Although both materials react with lithium within the same potential range of 3–0.01 V vs Li/Li^+, the exact potential for the maximal electrochemical activity differs for Co_3O_4 and Fe_2O_3. It can be seen in Figure 5a,b that, starting from the second cycles, two pronounced redox peaks appear in both cathodic and anodic scans. For both Co_3O_4–Fe_2O_3/C and Co_3O_4–Fe_2O_3 electrodes, there are peaks positioned at ~1.0 and ~0.8 V vs Li/Li^+ in the cathodic scan. They correspond to the reduction processes in Co_3O_4 and Fe_2O_3, respectively, dominating at these potentials. Indeed, a reduction peak is visible at ~0.77 V vs Li/Li^+ in the cathodic scan of Fe_2O_3/C material (Figure 5c) while a reduction peak at ~1.0–1.1 V can be seen in the CV of Co_3O_4/C. During the anodic scans of the hybrid Co_3O_4–Fe_2O_3/C electrode two oxidation peaks are visible at ~1.6 and 2.05 V vs Li/Li^+ in Figure 5b (and at ~1.7 and 2.03 V vs Li/Li^+ for the Co_3O_4–Fe_2O_3 electrode in Figure 5a). Again, this can be correlated with the maxima of oxidation processes in Fe_2O_3/C and Co_3O_4/C electrodes that happen at similar potentials (Figure 5c,d). The same indicative positions of redox peaks for Fe_2O_3 and Co_3O_4 can be found in the literature.[34,35] It follows from this analysis that the reduction and oxidation processes in the Co_3O_4 and Fe_2O_3 components of hybrid electrodes happens sequentially (with their maximal

DOI: 10.1021/acsami.5b05658
ACS Appl. Mater. Interfaces 2015, 7, 20736–20744

electrochemical redox activity at different potentials), which is accompanied by the sequential volume expansion and contraction in the Co_3O_4 and Fe_2O_3 components of the electrode. As a result, the development of stress in the electrode is subdued and the structural integrity of the hybrid electrode is retained (as shown in the SEM analysis of the optimal Co_3O_4–Fe_2O_3/C hybrid electrode in Figure 4b).

The in situ electrochemical properties of the hybrid Co_3O_4–Fe_2O_3 material are presented in Figure 6. The experiment was designed to track the phase changes in the electrode and a sample without carbon, Co_3O_4–Fe_2O_3 was selected to maximize the useful signal (the XRD signals from carbon-containing sample are relatively weaker and broader). During the in situ synchrotron XRD measurements the cell was cycled at a current density of 300 mA g^{-1} and the XRD data are shown in Figure 6. Li reacts first with Fe_2O_3 at ~1.12 V. The intensity of the Fe_2O_3 peak decreases with the decrease in cell potential and finally disappears at ~0.81 V. The intensity of the Co_3O_4 peaks began to decrease from 0.96 V and completely disappear at ~0.26 V. This is evident from Figure 6c where the (104) peak of Fe_2O_3 disappears first followed by the Co_3O_4 peaks. Figure 6b focuses on the Co_3O_4 (511) and (333) reflections during discharge illustrating their disappearance at around 102 min which corresponds to 0.71 V while Figure 6c shows the Co_3O_4 (220) and the Fe_2O_3 (104) reflections. The Fe_2O_3 reflection is essentially non-existent around 51 min or 0.81 V. Figure 6c clearly indicates that the Fe_2O_3 reflections disappear before the Co_3O_4 with a voltage difference of about 0.1 V between them. The disappearance of reflections implies that either there is a phase transformation and these phases are transforming into another phase, or there is a loss of crystallinity,[36] or the particles are becoming nanocrystallites.[37] In terms of the current electrode, it represents the loss of these crystalline phases. Figure 6d shows the charge process and essentially there are no changes to the patterns during charge. This suggests that once the crystalline phases disappear during first discharge they do not crystallize in the scale observable by XRD. It is most likely that these phases if they form are nanocrystalline and below the limit of detection for XRD. Note there is a slight increase in background in Figure 6d as these patterns are plotted with as-collected intensities. As the battery is charged, the background increases, and thus, there is a larger contribution to background from the charged products formed.

During electrochemical discharge/charge, the evolution of the phase fractions (relative) of the Fe_2O_3 and Co_3O_4 components as a function of time (Figure 7) and is directly correlated to the potential curve. It is observed that the sloping potential region is predominantly due to the Fe_2O_3 phase reacting during discharge and the plateau region signals the onset of the Co_3O_4 phase reacting. Notably, both phases disappear at the end of first discharge which, as suggested above, could be due to the formation of nanosized particles. Therefore, the Fe_2O_3 reacts first, followed by the Co_3O_4 component in the hybrid system. It is also worthwhile to note that the Co_3O_4 phase fraction remains stable while the majority of the Fe_2O_3 reacts and only begins to react at around 0.85 V. Therefore, we can directly show that each component starts being active at different parts of the first discharge and the activity appears to be sequential rather than simultaneous in their reactions in the first discharge of half-cell.

It is important to note that nanocrystalline intermediate phases may form for the Fe-containing component that continue to react during the Co_3O_4 reaction (in particular,

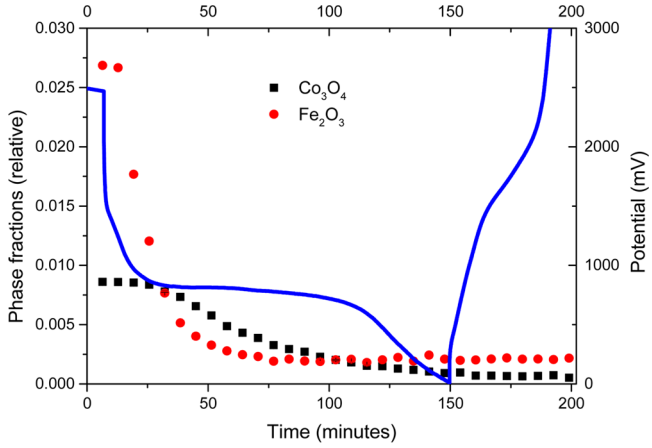

Figure 7. Evolution of the phase fractions of the Co_3O_4 and Fe_2O_3 components as a function of time correlated to the electrochemical charge/discharge curve in blue.

$Li_2(Fe_2O_3)$ has been suggested as a possible intermediate phase).[7] $Li_x[Co_3O_4]$, ($x \approx 0.2$–0.5) intermediate is expected to form during the corresponding transformation of Co_3O_4.[7] Having said that, we would like to note that we cannot conclude the nature of the intermediate phases from our experiments and we also do not have evidence that the intermediates remain the same in the second and following cycles. The suggested phases of $Li_2(Fe_2O_3)$ and $Li_x[Co_3O_4]$ are mentioned on the basis of previous in situ XRD studies conducted with larger Fe_2O_3 and Co_3O_4 crystallites. The hybrid electrode here consists of very small nanoscale particles of Fe_2O_3 and Co_3O_4, and their reactivity might deviate from the classical mechanisms.[38,39] Our Fe- and Co-containing intermediates are not observed with the XRD data which may be due to their amorphous or nanocrystalline nature for our nanosized sample. The subsequent reactivity of the intermediates is assumed to happen in the opposite order during the discharge (the CV graph in Figure 5a), and the peak of maximum electrochemical reactivity of iron oxide is at a lower potential (0.8 V vs Li/Li^+) than that of cobalt oxide (1.03 V vs Li/Li^+)).

Overall, our results indicate that, during the first discharge of the half-cell, iron oxide starts reacting with lithium first; however, the maximum of the electrochemical reaction happens for the iron oxide subsequently to the maximum of the electrochemical reaction for the cobalt oxide during normal cycling. It follows that electrochemical activities in the Fe_2O_3 and Co_3O_4 components of the hybrid electrode happen not simultaneously, but at different potentials for the two components, both during the initial stage of the intermediate phase formation and during the subsequent full conversion to metal nanoparticles and Li_2O. It is evident from CV graphs that similar sequential reactivity happens during the charge of the cells. The sequential reactivity of the oxide components leads to a better management of stress in the hybrid electrode. As we show in the SEM images of a hybrid electrode after 50 cycles (Figure 4b), it is possible to minimize electrode cracking and disintegration in such an electrode.

4. CONCLUSIONS

Significant improvements in the cycling stability and rate capability have been demonstrated in a hybrid electrode based on conversion reaction materials for Li-ion batteries. The

DOI: 10.1021/acsami.5b05658
ACS Appl. Mater. Interfaces 2015, 7, 20736–20744

hybrid Co_3O_4–Fe_2O_3/C electrode exhibits long-term cyclic stability (300 cycles) at a moderate current rate with a retained capacity of approximately 700 mAh g^{-1}. The reversible capacity of the Co_3O_4–Fe_2O_3/C electrode is still 400 mAh g^{-1} (above the theoretical capacity of graphite) at a high current rate of ca. 3 A g^{-1}, while other electrode materials used for comparison cannot perform well at such a high current rate. The attractive performance originates from the presence of percolating carbon host in the hybrid electrode and sequential volume expansion (and, as a result, better stress management) in the oxide components as confirmed by time-resolved in situ synchrotron X-ray diffraction combined with ex situ SEM analysis and cyclic voltammetry tests.

■ ASSOCIATED CONTENT

Supporting Information

The Supporting Information is available free of charge on the ACS Publications website at DOI: 10.1021/acsami.5b05658.

Methods for calculating the expected theoretical capacity and C-rates, additional data for TEM, charge–discharge, Coulombic efficiency, and overview of molten salts method. (PDF)

■ AUTHOR INFORMATION

Corresponding Authors

*E-mail: m.rahman@deakin.edu.au.

*E-mail: alexey.glushenkov@deakin.edu.au. Fax: +61352271103. Phone:+61352272642.

Notes

The authors declare no competing financial interest.

■ ACKNOWLEDGMENTS

Financial support from an Australian Postgraduate Award (APA) and Deakin University Central Research Grant Scheme, 2013, is acknowledged. Authors also acknowledge the use of electron microscopy facilities in the Victorian Node of the Australian National Fabrication Facility (ANFF) and thank Timcal, Ltd., for providing a sample of super P Li carbon black. The present work was carried out with the support of the Deakin Advanced Characterization Facility. AINSE Ltd is acknowledged for providing support through the Research Fellowship Scheme. Part of this research was undertaken on the Powder Diffraction beamline at the Australian Synchrotron, Victoria, Australia.

■ REFERENCES

(1) Dubal, D. P.; Ayyad, O.; Ruiz, V.; Gómez-Romero, P. Hybrid Energy Storage: The Merging of Battery and Supercapacitor Chemistries. *Chem. Soc. Rev.* **2015**, *44*, 1777–1790.

(2) Amatucci, G. G.; Badway, F.; Du Pasquier, A.; Zheng, T. An Asymmetric Hybrid Nonaqueous Energy Storage Cell. *J. Electrochem. Soc.* **2001**, *148*, A930–A939.

(3) Choi, H. S.; Im, J. H.; Kim, T. H.; Park, J. H.; Park, C. R. Advanced Energy Storage Device: A Hybrid Bat-Cap System Consisting of Battery-Supercapacitor Hybrid Electrodes Based on $Li_4Ti_5O_{12}$-Activated-Carbon Hybrid Nanotubes. *J. Mater. Chem.* **2012**, *22*, 16986–16993.

(4) Srivastava, M.; Singh, J.; Kuila, T.; Layek, R. K.; Kim, N. H.; Lee, J. H. Recent Advances in Graphene and Its Metal-Oxide Hybrid Nanostructures for Lithium-Ion Batteries. *Nanoscale* **2015**, *7*, 4820–4868.

(5) Poizot, P.; Laruelle, S.; Grugeon, S.; Dupont, L.; Tarascon, J. M. Nano-Sized Transition-Metal Oxides as Negative-Electrode Materials for Lithium-Ion Batteries. *Nature* **2000**, *407*, 496–499.

(6) Cabana, J.; Monconduit, L.; Larcher, D.; Palaćın, M. R. Beyond Intercalation-Based Li-Ion Batteries: The State of the Art and Challenges of Electrode Materials Reacting Through Conversion Reactions. *Adv. Mater.* **2010**, *22*, E170–E192.

(7) Reddy, M. V.; Subba Rao, G. V.; Chowdari, B. V. R. Metal Oxides and Oxysalts as Anode Materials for Li-Ion Batteries. *Chem. Rev.* **2013**, *113*, 5364–5457.

(8) Jiang, J. A.; Li, Y. Y.; Liu, J. P.; Huang, X. T. Building One-Dimensional Oxide Nanostructure Arrays on Conductive Metal Substrates for Lithium-Ion Battery Anodes. *Nanoscale* **2011**, *3*, 45–58.

(9) Li, L.; Seng, K. H.; Chen, Z.; Guo, Z.; Liu, H. K. Self-Assembly of Hierarchical Star-Like Co_3O_4 Micro/Nanostructures and Their Application in Lithium-Ion Batteries. *Nanoscale* **2013**, *5*, 1922–1928.

(10) Du, N.; Zhang, H.; Chen, B. D.; Wu, J. B.; Ma, X. Y.; Liu, Z. H.; Zhang, Y. Q.; Yang, D. R.; Huang, X. H.; Tu, J. P. Porous Co_3O_4 Nanotubes Derived From $Co_4(CO)_{12}$ Clusters on Carbon Nanotube Templates: A Highly Efficient Material for Li-Battery Applications. *Adv. Mater.* **2007**, *19*, 4505–4509.

(11) Larcher, D.; Masquelier, C.; Bonnin, D.; Chabre, Y.; Masson, V.; Leriche, J. B.; Tarascon, J. M. Effect of Particle Size on Lithium Intercalation into α-Fe_2O_3. *J. Electrochem. Soc.* **2003**, *150*, A133–A139.

(12) Chen, J.; Xu, L.; Li, W.; Gou, X. α-Fe_2O_3 Nanotubes in Gas Sensor and Lithium-Ion Battery Applications. *Adv. Mater.* **2005**, *17*, 582–586.

(13) Xiaodong, X.; Ruiguo, C.; Sookyung, J.; Cho, J. Spindle-Like Mesoporous α-Fe_2O_3 Anode Material Prepared From MOF Template for High-Rate Lithium Batteries. *Nano Lett.* **2012**, *12*, 4988–4991.

(14) Needham, S. A.; Wang, G. X.; Konstantinov, K.; Tournayre, Y.; Lao, Z.; Liu, H. K. Electrochemical Performance of Co_3O_4-C Composite Anode Materials. *Electrochem. Solid-State Lett.* **2006**, *9*, A315–A319.

(15) Nuli, N. Y.; Zhang, P.; Guo, Z. P.; Liu, H. K. Shape Evolution of α-Fe_2O_3 and Its Size-Dependent Electrochemical Properties for Lithium-Ion Batteries. *J. Electrochem. Soc.* **2008**, *155* (3), A196–A200.

(16) Lin, Y. M.; Abel, P. R.; Heller, A.; Mullins, C. B. α-Fe_2O_3 Nanorods as Anode Material for Lithium-Ion Batteries. *J. Phys. Chem. Lett.* **2011**, *2*, 2885–2891.

(17) Xue, X. Y.; Chen, Z. H.; Xing, L. L.; Yuan, S.; Chen, Y. J. SnO_2/α-MoO_3 Core-Shell Nanobelts and Their Extraordinarily High Reversible Capacity as Lithium-Ion Battery Anodes. *Chem. Commun.* **2011**, *47*, 5205–5207.

(18) Gu, X.; Chen, L.; Ju, Z.; Xu, H.; Yang, J.; Qian, Y. Controlled Growth of Porous α-Fe_2O_3 Branches on β-MnO_2 Nanorods for Excellent Performance in Lithium-Ion Batteries. *Adv. Funct. Mater.* **2013**, *23*, 4049–4056.

(19) Saadat, S.; Zhu, J.; Sim, D. H.; Hng, H. H.; Yazami, R.; Yan, Q. Coaxial Fe_3O_4/CuO Hybrid Nanowires as Ultra-Fast Charge/Discharge Lithium-Ion Battery Anodes. *J. Mater. Chem. A* **2013**, *1*, 8672–8678.

(20) Wu, H.; Xu, M.; Wang, Y.; Zheng, G. Branched Co_3O_4/Fe_2O_3 Nanowires as High Capacity Lithium-Ion Battery Anodes. *Nano Res.* **2013**, *6*, 167–173.

(21) Liu, X. H.; Liu, Y.; Kushima, A.; Zhang, S.; Zhu, T.; Li, J.; Huang, J. H. In-Situ TEM Experiments of Electrochemical Lithiation and Delithiation of Individual Nanostructures. *Adv. Energy Mater.* **2012**, *2*, 722–741.

(22) Rahman, M. M.; Glushenkov, A. M.; Ramireddy, T.; Tao, T.; Chen, Y. Enhanced Lithium Storage in Fe_2O_3-SnO_2-C Nanocomposite Anode with a Breathable Structure. *Nanoscale* **2013**, *5*, 4910–4916.

(23) Tao, T.; Glushenkov, A. M.; Zhang, C.; Zhang, H.; Zhou, D.; Guo, Z.; Liu, H. K.; Chen, Q.; Hu, H.; Chen, Y. MoO_3 Nanoparticles Dispersed Uniformly in Carbon Matrix: A High Capacity Composite Anode for Li-Ion Batteries. *J. Mater. Chem.* **2011**, *21*, 9350–9355.

(24) Brant, W. R.; Schmid, S.; Du, G.; Gu, Q.; Sharma, N. A. Simple Electrochemical Cell for *In-Situ* Fundamental Structural Analysis Using

DOI: 10.1021/acsami.5b05658
ACS Appl. Mater. Interfaces 2015, 7, 20736–20744

Synchrotron X-ray Powder Diffraction. *J. Power Sources* **2013**, *244*, 109−114.
(25) Gummow, R. J.; Sharma, N.; Feng, R.; Han, G.; He, Y. High Performance Composite Lithium-Rich Nickel Manganese Oxide Cathodes for Lithium-Ion Batteries. *J. Electrochem. Soc.* **2013**, *160*, A1856−A1862.
(26) Sharma, N.; Serras, P.; Palomares, V.; López del Amo, J. M.; Alonso, J.; Kubiak, P.; Fdez-Gubieda, M. L.; Rojo, T. Electrochemical Na Extraction/Insertion of $Na_3V_2O_{2x}(PO_4)_2F_{3-2x}$. *Chem. Mater.* **2013**, *25*, 4917−4925.
(27) Serras, P.; Palomares, V.; Rojo, T.; Brand, H. E. A.; Sharma, N. Structural Evolution of High Energy Density V^{3+}/V^{4+} Mixed Valent $Na_3V_2O_{2x}(PO_4)_2F_{3-2x}$ (x = 0.8) Sodium Vanadium Fluorophosphate Using In-Situ Synchrotron X-ray Powder Diffraction. *J. Mater. Chem. A* **2014**, *2*, 7766−7779.
(28) Pramudita, J. C.; Schmid, S.; Godfrey, T.; Whittle, T.; Alam, M.; Hanley, T.; Brand, H. E. A.; Sharma, N. Sodium Uptake in Cell Construction and Subsequent in Operando Electrode Behaviour of Prussian Blue Analogues, $Fe[Fe(CN)_6]_{1-x-y}H_2O$ and $FeCo(CN)_6$. *Phys. Chem. Chem. Phys.* **2014**, *16*, 24178−24187.
(29) Wallwork, K. S.; Kennedy, B. J.; Wang, D. The High Resolution Powder Diffraction Beamline for the Australian Synchrotron. *AIP Conf. Proc.* **2006**, 879−822.
(30) Larson, A. C.; Von Dreele, R. B. *General Structure Analysis System (GSAS)*. Los Alamos National Laboratory Report LAUR; Los Alamos National Laboratory: Los Alamos, NM, 1994, 86−748.
(31) Toby, B. H. EXPGUI, A Graphical User Interface for GSAS. *J. Appl. Crystallogr.* **2001**, *34*, 210−213.
(32) Xiong, Q. Q.; Xia, K. H.; Tu, J. P.; Chen, J.; Zhang, Y. Q.; Zhou, D.; Gu, C. D.; Wang, X. L. Hierarchical $Fe_2O_3@Co_3O_4$ Nanowire Array Anode for High-Performance Lithium-Ion Batteries. *J. Power Sources* **2013**, *240*, 344−350.
(33) Luo, Y.; Kong, D.; Luo, J.; Wang, Y.; Zhang, D.; Qiu, K.; Cheng, C.; Li, C. M.; Yu, T. Seed-Assisted Synthesis of $Co_3O_4@\alpha$-Fe_2O_3 Core-Shell Nanoneedle Arrays for Lithium-Ion Battery Anode with High Capacity. *RSC Adv.* **2014**, *4*, 13241−13249.
(34) Reddy, M. V.; Cherian, C. T.; Ramanathan, K.; Jie, K. C. W.; Daryl, T. Y. W.; Hao, T. Y.; Adams, S.; Loh, K. P.; Chowdari, B. V. R. Molten Synthesis of $ZnO{\cdot}Fe_3O_4$ and Fe_2O_3 and Its Electrochemical Performance. *Electrochim. Acta* **2014**, *118*, 75−80.
(35) Reddy, M. V.; Yu, C.; Jiahuan, F.; Loh, K. P.; Chowdari, B. V. R. Molten Salt Synthesis and Energy Storage Studies on $CuCo_2O_4$ and $CuO{\cdot}Co_3O_4$. *RSC Adv.* **2012**, *2*, 9619−9625.
(36) Sharma, N.; Du, G.; Studer, A. J.; Guo, Z.; Peterson, V. K. Structure of the MoS_2 Anode within a Li-Ion Battery During Discharge: In-Situ Neutron Diffraction Studies Using an Optimised Cell Design. *Solid State Ionics* **2011**, *199−200*, 37−43.
(37) Petkov, V.; Billinge, S. J. L.; Larson, P.; Mahanti, S. D.; Vogt, T.; Rangan, K. K.; Kanatzidis, M. G. Structure of Nanocrystalline Materials Using Atomic Pair Distribution Function Analysis: Study of $LiMoS_2$. *Phys. Rev. B: Condens. Matter Mater. Phys.* **2002**, *65*, 092105.
(38) Larcher, D.; Sudant, G.; Leriche, J. B.; Chabre, Y.; Tarascon, J. M. The Electrochemical Reduction of Co_3O_4 in a Lithium Cell. *J. Electrochem. Soc.* **2002**, *149*, A234−A241.
(39) Larcher, D.; Bonnin, D.; Cortes, R.; Rivals, I.; Personnaz, L.; Tarascon, J. M. Combined XRD, EXAFS, and Mössbauer Studies of the Reduction by Lithium of α-Fe_2O_3 with Various Particle Sizes. *J. Electrochem. Soc.* **2003**, *150*, A1643−A1650.

DOI: 10.1021/acsami.5b05658
ACS Appl. Mater. Interfaces 2015, 7, 20736−20744